

---

# Fine-Grained Cross-View Localization via Local Feature Matching and Monocular Depth Priors

---

Zimin Xia\*

Chenghao Xu\*

Alexandre Alahi

École Polytechnique Fédérale de Lausanne (EPFL), Switzerland  
{zimin.xia, chenghao.xu, alexandre.alahi}@epfl.ch

## Abstract

We propose an accurate and highly interpretable fine-grained cross-view localization method that estimates the 3 Degrees of Freedom pose of a ground-level image by matching its local features with a reference aerial image. Previous methods typically transform the ground image into a bird’s-eye view (BEV) representation and then align it with the aerial image for localization. However, this transformation often leads to information loss due to perspective distortion or compression of height information, thereby degrading alignment quality with the aerial view. In contrast, our method directly establishes correspondences between ground and aerial images and lifts only the matched keypoints to BEV space using monocular depth prior. Notably, modern depth predictors can provide reliable metric depth when the test samples are similar to the training data. When the depth distribution differs, they still produce consistent relative depth, i.e., depth accurate up to an unknown scale. Our method supports both metric and relative depth. It employs a scale-aware Procrustes alignment to estimate the camera pose from the correspondences and optionally recover the scale when using relative depth. Experimental results demonstrate that, with only weak supervision on camera pose, our method learns accurate local feature correspondences and achieves superior localization performance under challenging conditions, such as cross-area generalization and unknown orientation. Moreover, our method is compatible with various relative depth models without requiring per-model finetuning. This flexibility, combined with strong localization performance, makes it well-suited for real-world deployment.

## 1 Introduction

Visual localization, a fundamental task in computer vision and mobile robotics, aims to estimate the camera pose with respect to a representation of the environment [42]. In dense urban areas, specialized positioning sensors, such as Global Navigation Satellite System (GNSS), have errors up to tens of meters [53]. Fine-grained cross-view localization, a recently emerging task, offers a promising complement. It estimates the 3 Degrees of Freedom (DoF) camera pose, i.e., 2D planar location and yaw orientation, by comparing its captured ground-level images to an aerial image of the surroundings, identified using the noisy position estimates from GNSS.

Previous approaches tackle the cross-view localization task with various formulations, such as matching global image descriptors [55], sliding ground-view transformed bird’s-eye-view (BEV) features over aerial images [7], and estimating homography [51]. Significant effort has been devoted to how to aggregate information along the vertical (height) axis to transform the ground-view feature

---

\*Equal contribution.

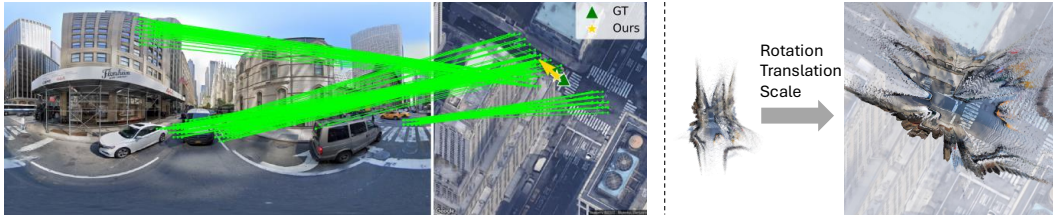


Figure 1: Our method addresses fine-grained cross-view localization by matching local features between ground and aerial images. Using the depth from a monocular depth predictor, we lift only the matched ground keypoints to BEV space, and then jointly compute rotation, translation, and scale using these correspondences to align the BEV points with the aerial image. Our image matching is learned through weak supervision from the camera pose.

to BEV, such that the resulting BEV can align well with aerial imagery. [38] designs a learned module to refine the distortion caused by above-ground objects in homography. [50] uses attention to gather information from above-ground objects, while [52] explicitly classifies features along height.

However, transforming the ground image to BEV still inevitably leads to information loss, as it may introduce ray-directional distortions on objects [38], or the model must discard or compress information along height [52, 50]. These limitations can degrade the semantic richness of the BEV feature, thereby impairing its alignment with aerial imagery. In contrast, we propose to directly establish correspondences between ground and aerial images, without explicitly selecting features along height. The correspondence between ground and aerial views is inherently many-to-one: rather than restricting the match of a rooftop in the aerial image to only the top of a building facade in the ground view, the entire facade can contribute to this association. On the one hand, the topmost point may not exhibit similar appearance in the aerial view. On the other hand, image matching has evolved beyond identifying visually similar content to capturing semantically consistent correspondences, as evidenced in visual grounding [18, 56, 57] and cross-domain visual matching [30].

After matching image-plane correspondences, an intuitive approach to computing the 3-DoF camera pose is to propagate the correspondences into a shared BEV space. To directly bridge the ground view and BEV, previous methods rely on LiDAR [15, 49] or monocular depth models [47]. Since LiDAR is not widely available, we opt for a vision-based solution. Recent monocular depth models [58, 59, 27, 46] provide accurate metric depth when test scenes resemble their training distribution. When generalizing to a new distribution, absolute depth may be ambiguous, but these models still yield reliable non-metric relative depth, i.e., depth up to an unknown scale. This relative depth is still highly valuable, as it preserves the scene’s spatial structure. Notably, when humans self-localize using Google Satellite Maps [11], they often explicitly match co-visible contents, e.g., road markings and buildings, across views, and then leverage the relative geometry of objects to find the ego-location, a process now replicated by our method. As shown in Fig. 1, our proposed method first identifies sparse correspondences between ground and aerial images, uses a monocular depth prior to map the matched ground keypoints into the BEV space, and employs scale-aware Procrustes alignment [43] to compute the rotation, translation and scale, between the BEV and aerial image.

Concretely, our main contributions are: (1) We propose a simple and accurate fine-grained cross-view localization method that matches local features across views. Our method achieves superior localization accuracy under challenging conditions, such as cross-area generalization and unknown orientation. On the KITTI cross-area test set, it reduces the mean localization error by 26% compared to the previous state-of-the-art. (2) Our method establishes accurate correspondences between ground and aerial images. By analytically computing the pose from these correspondences, it delivers highly interpretable localization results. The feature matching is learned without explicit labels, relying only on weak supervision from the camera pose. (3) At inference time, our method is plug-and-play with different relative depth predictors, requiring no finetuning and resulting in only a minor drop in localization accuracy. Once reliable correspondences with the metric aerial imagery are established, our method can recover the scale of the relative depth.

## 2 Related Work

**Fine-grained cross-view localization** is a challenging task due to the drastically different viewpoints and the varying times at which ground and aerial images are captured. State-of-the-art approaches tackle this domain gap primarily by learning a deep network for camera pose estimation. Global descriptor-based methods [54, 16, 55] leverage contrastive learning to pull the ground and aerial features to a common representation space, and compare the ground image descriptor to aerial descriptors extracted at different candidate poses. Geometry transformation-based methods [7, 48, 34, 50, 38, 37, 51, 6, 52] first warp the ground image into a BEV representation, and then either perform a sliding-window search over the aerial image to find the best alignment [34, 7, 37] or estimate the relative pose by directly matching features between the BEV and aerial view [38, 51, 48, 50, 52]. Despite the increasing localization accuracy, most methods do not explicitly identify matched local features across views, offering limited interpretability. A recent work [52] demonstrated, for the first time, the ability to find ground-aerial local feature correspondences by defining a dense 3D voxel space and querying image features for each voxel. However, this process is inefficient due to the sparse nature of 3D space, and this method performs poorly when camera orientation is unknown.

**Ground-view visual localization** typically follows a highly interpretable pipeline [32, 35], which involves finding local image feature correspondences [33, 41] and then estimating camera pose using a geometry-based solver [17]. However, this pipeline becomes challenging in the cross-view setting due to the significant domain gap and the lack of labeled correspondences. We propose to learn such correspondences for cross-view localization without labels, facilitated by monocular depth priors.

**Monocular depth estimation** bridges 2D imagery and 3D scene. Early methods [19, 9, 21, 31] demonstrated strong performance in predicting reliable depth on in-domain data. Later, unified loss functions and architectures [28, 29] enabled joint training on diverse datasets [10, 20, 23, 40], making generalizable relative depth prediction possible, i.e., estimating depth values that are accurate up to an unknown scale [46, 59]. By finetuning on ground-truth depth, these methods can also produce accurate metric depth, i.e., depth values in absolute metric space [58, 59, 2]. Recently, training depth models with camera-awareness [62, 60, 13, 39, 26, 27] has further advanced the feasibility of generalizable metric depth prediction. Considering all the variations of depth models, we design our cross-view localization method to support both metric and relative depth. The metric depth provides guidance on learning accurate local feature matching. Once trained, our model can operate in a plug-and-play manner at inference time with various depth predictors, including relative depth ones.

## 3 Methodology

Fine-grained cross-view localization aims to estimate the 3-DoF pose, i.e., the 2D metric location  $\mathbf{t} \in \mathbb{R}^2$  and yaw orientation  $\phi \in [-\pi, \pi)$ , of a ground-level image  $G$  by matching it to a geo-referenced aerial image  $A$  covering the local surrounding area.

### 3.1 Motivation

Our goal is to solve fine-grained cross-view localization via local feature matching. Since existing datasets lack ground-truth correspondences between ground and aerial images, we learn the matching in a weakly supervised manner using only the pose. To support this process, we incorporate a pre-trained monocular depth model to predict a depth map of the ground image, i.e.,  $D = \mathcal{D}(G)$ .

Importantly, monocular depth prediction is a geometrically ill-posed problem, as there is no unique mapping from a single image to absolute metric depth. State-of-the-art methods either learn generalizable metric depth prediction from diverse training data [27, 26, 62], or predict depth that is accurate only up to a per-image unknown scale [46, 58].<sup>2</sup> Therefore, our method is designed to use relative depth, while it also supports metric depth when available. Notably, different depth predictors can be seamlessly integrated into our method at inference time without the need for finetuning or retraining.

As shown in Fig. 2, our method employs two feature extraction branches sharing the same architecture. Each branch includes a frozen pre-trained DINOv2 encoder [25] followed by a lightweight projection

---

<sup>2</sup>Recent work [61] also explored modeling the relationship between relative and metric depth using a scale and a shift. As our goal is not metric depth prediction, we follow [5, 4] and consider only the scale for simplicity.

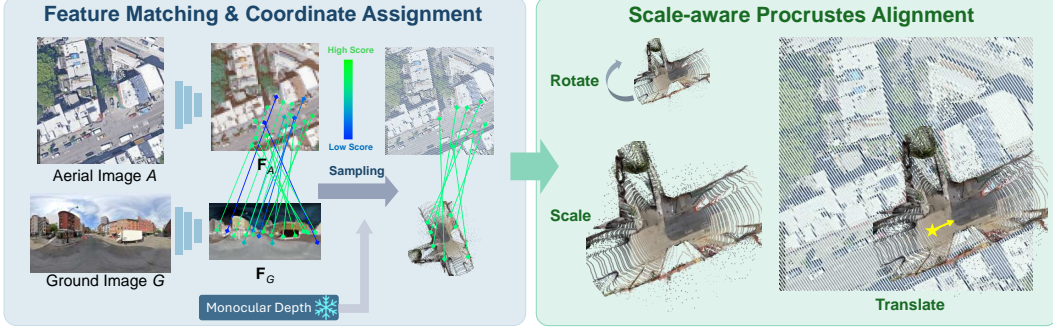


Figure 2: Our method first matches local features between ground and aerial images. The sampled correspondences are then lifted to the BEV space using monocular depth priors. By aligning these correspondences using scale-aware Procrustes alignment, we estimate the rotation, translation, and scale between the ground and aerial views.

head, composed of several convolutional layers and a self-attention layer [44]. The branches map the ground image  $G$  and aerial image  $A$  to local image feature maps  $\mathbf{F}_G$  and  $\mathbf{F}_A$ , respectively.

### 3.2 Pose Estimation

Given the ground and aerial feature maps  $\mathbf{F}_G$  and  $\mathbf{F}_A$ , our goal is to estimate the 3-DoF metric camera pose by establishing correspondences between them. We first perform feature matching between  $\mathbf{F}_G$  and  $\mathbf{F}_A$ , and subsequently leverage pre-trained monocular depth models to assign coordinates to the correspondences, which are then used to estimate the camera pose. Notably, reliable depth predictors are now available for both perspective images [46, 59] and panoramic images [46, 27].

**Matching:** We first compute the pairwise matching scores,  $M$ , between aerial and ground features  $\mathbf{F}_A$  and  $\mathbf{F}_G$  based on cosine similarity,  $M = \text{cosine}(\mathbf{F}_A, \mathbf{F}_G)/\tau$ , where  $\tau$  is a temperature parameter. Following [3, 33], we append a learnable dustbin to both the rows and columns of  $M$ , allowing the model to reject uncertain or unmatched keypoints. On this extended matching score matrix  $M^*$ , we apply dual softmax normalization over rows and columns to obtain a match probability matrix  $\hat{M}^*$ ,

$$\hat{M}_{ij}^* = \frac{e^{M_{ij}^*}}{\sum_k e^{M_{ik}^*}} \cdot \frac{e^{M_{ij}^*}}{\sum_l e^{M_{lj}^*}}. \quad (1)$$

Finally, we drop the dustbin row and column from  $\hat{M}^*$ , and sample  $N$  correspondences for pose estimation. We denote the matching probability of the sampled correspondences as  $w_n$ ,  $n \in [1, \dots, N]$ , which will be used as the weight in the Procrustes alignment.

**Coordinate assignment:** Given the  $N$  sampled correspondences, we denote the metric coordinates of the 2D point associated with the  $n$ -th aerial feature as  $(x_n^A, y_n^A)$ , with the origin defined at the center of the aerial image. For the corresponding ground feature, we retrieve its depth from  $D$  and use its associated ray direction to compute its 3D location in space. The resulting 3D point is denoted as  $(x_n^G, y_n^G, z_n^G)/s$ , with the origin defined at the ground camera. Here,  $s$  is an unknown scale factor from the ground coordinate system to the aerial metric space, and  $s = 1$  when a reliable metric depth model is used. As motivated in Sec. 1, we retain all matched ground points without explicitly selecting them based on their height (z-coordinate). Our experiments will show that explicitly selecting the topmost point does not improve performance.

**Scale-aware Procrustes alignment:** As shown in Fig. 2 right, once we have the point correspondences  $\{(x_n^A, y_n^A), (x_n^G, y_n^G, z_n^G)/s\}$ , and their matching probabilities  $w_n$ , the rotation  $\mathbf{R}$ , translation  $\mathbf{t}$ , and the scale  $s$  between the ground points and the metric space aerial points can be computed analytically in a differentiable manner using 2D scale-aware Procrustes alignment [43]<sup>3</sup>.

For simplicity, we denote the planar coordinates of all ground points as  $\mathbf{P} = \mathbf{P}^*/s$ , assuming they differ from the metric coordinates,  $\mathbf{P}^* = \{(x_1^G, y_1^G), \dots, (x_n^G, y_n^G)\}$ , by an unknown scale  $s$ . The

<sup>3</sup>In [52, 1], all coordinates are in metric space, so they use orthogonal Procrustes [12] and ignore scale.

coordinates of all aerial points are denoted as  $\mathbf{Q}$ . The objective is to estimate the scale  $s$ , rotation matrix  $\mathbf{R}$  and metric translation  $\mathbf{t}$  that satisfy the transformation  $\mathbf{Q} = s(\mathbf{R} \cdot \mathbf{P}) + \mathbf{t}$ .

First, we compute the weighted centroids of the aerial and ground point sets,

$$\bar{\mathbf{Q}} = \frac{1}{W} \sum_{n=1}^N w_n \mathbf{Q}_n, \quad \bar{\mathbf{P}} = \frac{1}{W} \sum_{n=1}^N w_n \mathbf{P}_n, \quad \text{with } W = \sum_{n=1}^N w_n. \quad (2)$$

In Eq. 2, the better matched points will contribute more to the centroids of the point sets. Then, we center the point sets and compute their covariance matrix,

$$\tilde{\mathbf{Q}} = \mathbf{Q} - \bar{\mathbf{Q}}, \quad \tilde{\mathbf{P}} = \mathbf{P} - \bar{\mathbf{P}}, \quad \mathbf{C} = \sum_{n=1}^N w_n \left( \tilde{\mathbf{P}}_n \right) \left( \tilde{\mathbf{Q}}_n \right)^\top, \quad (3)$$

where  $\tilde{\mathbf{P}}_n$  and  $\tilde{\mathbf{Q}}_n$  are the  $n$ -th points in the centered point sets  $\tilde{\mathbf{Q}}$  and  $\tilde{\mathbf{P}}$ . The covariance matrix  $\mathbf{C}$  captures how the centered ground points relate to the centered aerial points, encoding the direction and strength of their mutual variation.

Next, we perform Singular Value Decomposition (SVD) on  $\mathbf{C}$ ,  $\mathbf{C} = \mathbf{U}\mathbf{\Sigma}\mathbf{V}^\top$ , and the optimal rotation can be recovered as  $\mathbf{R} = \mathbf{V}\mathbf{U}^\top$ , which derives the estimated yaw orientation  $o$ . The scale and translation from the ground points  $\mathbf{P}$  to the aerial points  $\mathbf{Q}$  is then computed as,

$$s^* = \frac{\text{Tr}(\mathbf{\Sigma})}{\sum_{n=1}^N w_n \|\tilde{\mathbf{P}}_n\|^2}, \quad \mathbf{t} = \bar{\mathbf{Q}} - s^*(\mathbf{R} \cdot \bar{\mathbf{P}}). \quad (4)$$

Recall that  $\mathbf{P} = \mathbf{P}^*/s$ . Substituting this into Eq. 4, the estimated scale  $s^*$  can be rewritten in terms of the (unscaled) metric coordinates  $\mathbf{P}^*$ , with  $\mathbf{\Sigma}^*$  denoting the singular value matrix computed from the SVD between  $\mathbf{Q}$  and  $\mathbf{P}^*$ :

$$s^* = \frac{\text{Tr}(\mathbf{\Sigma}^*/s)}{\sum_{n=1}^N w_n \|\tilde{\mathbf{P}}_n^*/s\|^2} = \frac{\text{Tr}(\mathbf{\Sigma}^*)/s}{\sum_{n=1}^N w_n \|\tilde{\mathbf{P}}_n^*\|^2 / s^2} = \frac{s \text{Tr}(\mathbf{\Sigma}^*)}{\sum_{n=1}^N w_n \|\tilde{\mathbf{P}}_n^*\|^2}. \quad (5)$$

Since  $\mathbf{P}^*$  lies in the same metric space as the aerial points  $\mathbf{Q}$ , and there is no scale difference between them, we have  $\text{Tr}(\mathbf{\Sigma}) = \sum_{n=1}^N w_n \|\tilde{\mathbf{P}}_n\|^2$ . This leads to  $s^* = s$ , indicating that the ground points  $\mathbf{P}$  must be scaled by  $s$  to align them with the metric aerial points  $\mathbf{Q}$ .

**Practical implication:** This derivation shows that, regardless of the unknown scale of the ground points, scale-aware Procrustes alignment yields a consistent estimate of the camera pose and can recover the scale  $s$ . Its differentiability makes it particularly well-suited for learning local feature matching through pose supervision, while also enabling inference using only relative depth.

**Assumptions:** In practice, the implication holds only when the transformation between aerial and ground points is an exact similarity transform. On the one hand, it requires that the depth prior and scene geometry are well-aligned, i.e., the relative depth estimated from the ground image must correspond to the aerial layout, and the scene geometry must be sufficiently structured to support stable alignment. On the other hand, the estimated correspondences must be highly accurate. Assuming that relative depth predictions are generally reliable, we focus on learning accurate correspondences. Our experiments demonstrate that, once accurate local feature correspondences are established, our model can consistently estimate pose, even when different scales are applied to the ground points.

### 3.3 Model Supervision

We follow [52] to provide supervision on both the pose and correspondences. For camera pose, we adopt the Virtual Correspondence Error (VCE) loss from [52]. Specifically, we define a set of  $N_v$  virtual points  $\mathbf{P}_v$  in a 2D metric space, where the hyperparameter  $l$  controls the spatial extent of the space. We apply both the ground-truth transformation,  $\mathbf{R}_{\text{gt}}, \mathbf{t}_{\text{gt}}$ , and the estimated transformation,  $\mathbf{R}, \mathbf{t}$ , to these virtual points. The loss  $\mathcal{L}_{\text{VCE}}$  then minimizes the mean Euclidean distance between the corresponding transformed points,

$$\mathcal{L}_{\text{VCE}} = \frac{1}{N_v} \sum \|\mathbf{R}_{\text{gt}} \cdot \mathbf{P}_v + \mathbf{t}_{\text{gt}} - (\mathbf{R} \cdot \mathbf{P}_v + \mathbf{t})\|_2. \quad (6)$$

When metric depth is available during training, we use the ground-truth pose to find, for the ground points, their corresponding aerial points and compute an infoNCE loss [24],  $\mathcal{L}_{G2S}$ , to encourage these correspondences. We also find, for the aerial points, their corresponding ground points. However, multiple ground points may exist at different heights but share similar BEV locations. We select the ground point closest to the projected location and compute the  $\mathcal{L}_{S2G}$ , using only ground points outside a defined local neighborhood as negatives. Therefore, we do not limit the matching between aerial and ground images to be one-to-one. The detailed formulation is provided in the Appendix. The total loss is then a weighted combination of the VCE loss and infoNCE losses,  $\mathcal{L} = \mathcal{L}_{VCE} + \beta(\mathcal{L}_{G2S} + \mathcal{L}_{S2G})/2$ .

## 4 Experiment

We first introduce the datasets and metrics, followed by implementation details. We then compare our method with previous state-of-the-art vision-based methods and showcase our inference using different monocular depth predictors. Next, we present qualitative results and our ablation study.

### 4.1 Datasets and Evaluation Metrics

**KITTI** [10] provides forward-facing ground-level images with a limited field of view. Aerial images for KITTI were collected by [36], who also split the dataset into Training, Test1, and Test2 subsets. Test1 includes images from the same region as the Training set, while Test2 contains images from a different region. We refer to Test1 and Test2 as the same-area and cross-area test sets, respectively. KITTI provides ground-truth depth maps, which are commonly used in training depth foundation models [59, 58]. We use the metric depth predictions from [59] for our experiments on KITTI.

**VIGOR** [63] is a widely used cross-view localization dataset, containing ground-level panoramas and aerial images from four U.S. cities. It provides two splits: same-area and cross-area. In the same-area split, training and test images are collected from all four cities, while in the cross-area split, the training and test sets come from two different cities. VIGOR does not have ground-truth depth. During training, we adopt a recent metric depth model [27], which has shown strong performance on outdoor panoramic images. At test time, we report results using both this metric depth and relative depth from various methods [46, 14, 45]. Additionally, we include results in the Appendix where both training and testing are performed using only relative depth.

**Metrics:** We report the mean and median localization and orientation errors. For KITTI, we further decompose localization errors into longitudinal and lateral components based on the driving direction, and report the percentage of samples within the defined error thresholds.

### 4.2 Implementation Details

For both datasets, we use AdamW [22] with a learning rate of  $1 \times 10^{-4}$ . Training is conducted on a single H100 GPU with a batch size of 80 for VIGOR and 224 for KITTI. We follow the setting from [52]: the temperature parameter  $\tau$  in matching score computation is set to 0.1, the aerial feature map  $\mathbf{F}_A$  is resized to generate  $41 \times 41$  aerial points,  $\mathcal{L}_{VCE}$  uses  $N_v = 10 \times 10$  points, with  $l$  set to 5 m, and  $N = 1024$  correspondences are sampled for pose estimation. For  $\mathcal{L}_{S2G}$ , negatives are 1 m away in planar distance from the projected location. We use  $\beta = 1$  for VIGOR and  $\beta = 0.1$  for KITTI. During testing on VIGOR, we use RANSAC [8] for outlier filtering. RANSAC is not used on KITTI, as we did not observe any improvement in localization accuracy. When using metric depth, we apply a maximum depth threshold of 35 m for VIGOR and 40 m for KITTI, setting the matching score in  $\hat{M}^*$  to zero for points exceeding this threshold. For relative depth predictors, we apply a fixed initial scale (identified by visually inspecting a few examples) to all relative depth maps and then use the threshold to filter out matches corresponding to sky and distant objects.

### 4.3 Quantitative Results

**KITTI:** As shown in Tab. 1, our method significantly outperforms previous state-of-the-art methods on the cross-area test set, while achieving slightly higher localization error on the same-area test set. When test samples are from a different area than training, our method lowers the mean localization error by 26% (from 7.45 m to 5.51 m) compared to previous state-of-the-art [52], demonstrating stronger generalization capability. Our orientation error is slightly higher than that of the baselines.

Table 1: KITTI test results. **Best in bold.** During both training and testing, our method utilizes metric depth predictions from DepthAnythingv2 [59].

	Methods	↓ Loc. (m)		↑ Lateral (%)		↑ Long. (%)		↓ Orient. (°)		↑ Orient. (%)	
		Mean	Median	R@1m	R@5m	R@1m	R@5m	Mean	Median	R@1°	R@5°
Same-area	GGCVT [37]	-	-	76.44	98.89	23.54	62.18	-	-	<b>99.10</b>	<b>100.00</b>
	CCVPE [55]	1.22	0.62	97.35	99.71	77.13	97.16	0.67	0.54	77.39	99.95
	HC-Net [51]	0.80	0.50	99.01	99.73	<b>92.20</b>	<b>99.25</b>	<b>0.45</b>	0.33	91.35	99.84
	DenseFlow [38]	1.48	<b>0.47</b>	95.47	99.79	87.89	94.78	0.49	<b>0.30</b>	89.40	99.31
	FG <sup>2</sup> [52]	<b>0.75</b>	0.52	<b>99.73</b>	<b>100.00</b>	86.99	98.75	1.28	0.74	61.17	95.65
	Ours	1.11	0.76	99.60	<b>100.00</b>	65.86	98.04	1.97	1.43	36.68	92.84
Cross-area	GGCVT [37]	-	-	57.72	91.16	14.15	45.00	-	-	<b>98.98</b>	<b>100.00</b>
	CCVPE [55]	9.16	3.33	44.06	90.23	23.08	64.31	<b>1.55</b>	<b>0.84</b>	57.72	96.19
	HC-Net [51]	8.47	4.57	75.00	97.76	<b>58.93</b>	<b>76.46</b>	3.22	1.63	33.58	83.78
	DenseFlow [38]	7.97	3.52	54.19	91.74	23.10	61.75	2.17	1.21	43.44	89.31
	FG <sup>2</sup> [52]	7.45	4.03	89.46	<b>99.80</b>	12.42	55.73	3.33	1.88	30.34	81.17
	Ours	<b>5.51</b>	<b>2.97</b>	<b>90.97</b>	99.22	13.70	65.06	3.32	2.12	26.03	80.68

Notably, models that directly regress orientation [37, 55, 38, 51] perform well on KITTI, as most forward-facing ground images align with the road direction, an implicit prior that these models can easily learn. In contrast, our method computes orientation analytically from local feature correspondences, which makes it harder to exploit this prior but offers greater interpretability.

**VIGOR:** Overall, our method demonstrates strong and consistent performance across all settings, including known/unknown orientations and same-/cross-area scenarios, see Tab. 2. For example, while FG<sup>2</sup> achieves lower localization error when the orientation is known, our method significantly outperforms it in the more challenging unknown orientation setting. This highlights our model’s practical applicability in real-world scenarios where camera orientation is not available. Compared to the previous state-of-the-art under unknown orientation [55], our method achieves comparable localization accuracy: slightly higher mean error on the same-area test set, but lower mean error on the cross-area test set. Notably, our method consistently achieves the lowest mean orientation error across all settings, demonstrating its effectiveness in jointly estimating both location and orientation.

Table 2: VIGOR test results. **Best in bold.** During training, we use metric depth predictions from Unik3D [27]. The row ‘ours’ reports test results using metric depth from the same model. The rows labeled ‘ours-xxx’ present the test results of our trained model combined with different relative depth input. ‘Ours-Unik3D<sub>rel</sub>’ represents the case where we manually scale the metric depth by an arbitrary factor. The relative depth predictors, BiFuse++[45] and UniFuse[14], are provided by [46].

Ori.	Methods	Same-area				Cross-area			
		↓ Localization (m)		↓ Orientation (°)		↓ Localization (m)		↓ Orientation (°)	
		Mean	Median	Mean	Median	Mean	Median	Mean	Median
Known	SliceMatch [16]	5.18	2.58	-	-	5.53	2.55	-	-
	CCVPE [55]	3.60	1.36	-	-	4.97	1.68	-	-
	GGCVT [37]	4.12	1.34	-	-	5.16	1.40	-	-
	DenseFlow [38]	3.03	<b>0.97</b>	-	-	5.01	2.42	-	-
	HC-Net [51]	2.65	1.17	-	-	3.35	1.59	-	-
	FG <sup>2</sup> [52]	<b>1.95</b>	1.08	-	-	<b>2.41</b>	<b>1.37</b>	-	-
	Ours	3.06	1.59	-	-	3.43	1.90	-	-
	Ours-Unik3D <sub>rel</sub>	3.06	1.59	-	-	3.43	1.90	-	-
	Ours-BiFuse++	3.17	1.69	-	-	3.56	2.02	-	-
	Ours-UniFuse	3.14	1.67	-	-	3.54	2.01	-	-
Unknown	SliceMatch [16]	6.49	3.13	25.46	4.71	7.22	3.31	25.97	4.51
	CCVPE [55]	<b>3.74</b>	<b>1.42</b>	12.83	6.62	5.41	<b>1.89</b>	27.78	13.58
	DenseFlow [38]	4.97	1.90	11.20	<b>1.59</b>	7.67	3.67	17.63	2.94
	FG <sup>2</sup> [52]	8.95	7.32	15.02	2.94	10.02	8.14	31.41	5.45
	Ours	3.94	1.78	<b>9.54</b>	2.00	<b>4.23</b>	2.09	<b>11.67</b>	<b>2.21</b>
	Ours-Unik3D <sub>rel</sub>	3.94	1.78	<b>9.54</b>	2.00	<b>4.23</b>	2.09	<b>11.67</b>	<b>2.21</b>
	Ours-BiFuse++	4.12	1.94	10.13	2.31	4.43	2.26	12.27	2.47
	Ours-UniFuse	4.03	1.89	9.81	2.21	4.36	2.21	12.10	2.43

**Inference with relative depth:** As noted in Sec. 3.2, scale-aware Procrustes alignment is theoretically guaranteed to yield a consistent pose estimate regardless of the scaling applied to the ground points. In practice, however, this assumption may not hold due to imperfect matching. To assess this, we experimentally evaluate the consistency of the estimated pose under varying ground point scales. Specifically, we conduct two additional evaluations on the VIGOR same-area and cross-area test sets using our trained models. In the first setting, we apply arbitrary scale factors to the metric depth predicted by [27] to evaluate the consistency of our pose estimation. We vary the scale from 0.001 to 1000 and observe that the resulting variation in both mean and median localization error remains below 1 cm (‘Ours-Unik3D<sub>rel</sub>’ in Tab. 2), demonstrating strong scale invariance. This robustness is due to both the accurate correspondence matching and the spatial distribution of the matched points.

Second, we evaluate a more practical scenario where only a relative depth model [45, 14, 46] is available in inference. We use different relative depth models in a plug-and-play manner with our estimated correspondences, without retraining or finetuning our model for relative depth. As shown in the bottom two rows of the known and unknown orientation entries in Tab. 2, using relative depth leads to only a modest increase, less than 0.2 m, in localization error, regardless of whether the evaluation is conducted in same-area or cross-area scenarios. This flexibility in incorporating different depth predictors highlights the practicality and robustness of our method for real-world deployment.

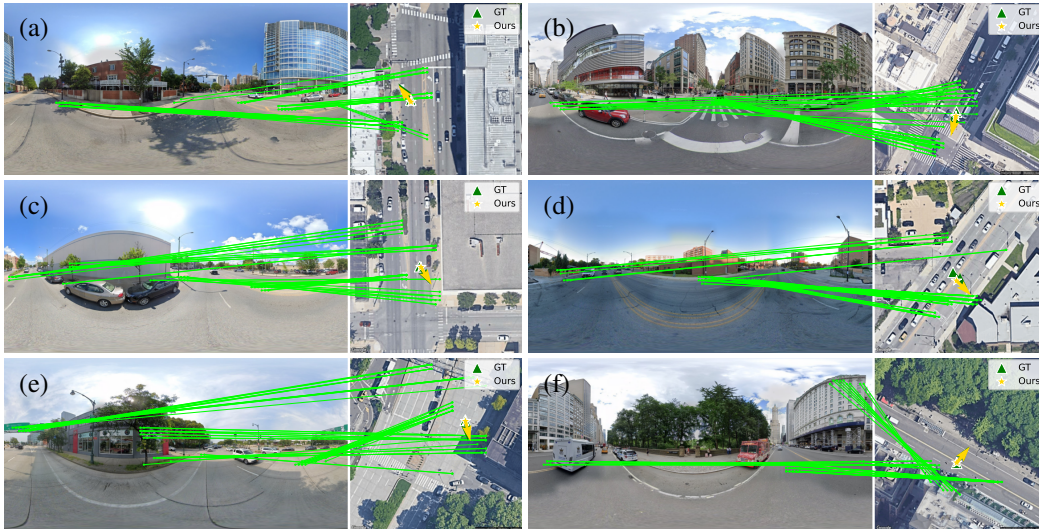


Figure 3: Local feature matching results on the VIGOR same-area test set under unknown orientation. We visualize the top 50 correspondences, ranked by matching score.

#### 4.4 Qualitative Results

**Local feature matching:** The core of our accurate and robust localization lies in the reliability of our correspondence matching between ground and aerial images. Among existing methods, only our approach and FG<sup>2</sup> [52] are capable of producing such local feature correspondences, providing superior interpretability. However, FG<sup>2</sup> fails when the orientation of the camera is unknown.

We show in Fig. 3 examples of our local feature matching. As shown in (a) and (b), our method accurately matches road markings, such as yellow grid lines and text painted on the road surface, across ground and aerial views. In (c) and (d), our method uses streetlights as landmarks to anchor positions and establish correspondences between views. Interestingly, in (e), our method matches an overhead road sign in the ground view to its shadow in the aerial image, demonstrating that the matching is not solely appearance-based but reflects strong semantic understanding. Finally, (f) highlights that, without constraining ground keypoints to lie on object tops, our method establishes reasonable matches between building facades in the ground view and their rooftops in the aerial view.

**Scale recovery:** Next, we demonstrate that when a relative depth predictor [45] is used in inference, our method can jointly estimate the camera pose and the scale between the relative depth and the aerial metric space. Fig. 4 shows the alignment by overlaying the rotated, translated, and scaled BEV points onto the aerial image using the estimations. The transformed points show consistent alignment with the aerial imagery, highlighting the accuracy of both the estimated pose and scale.

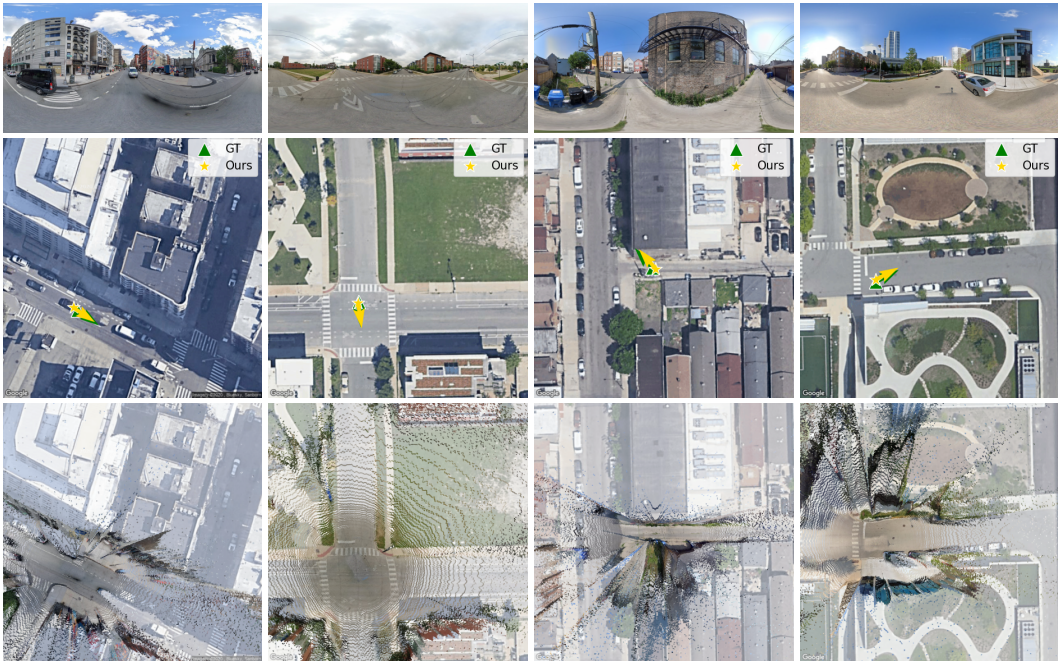


Figure 4: BEV points overlaid on the aerial image after applying the predicted rotation, translation, and scale transformations.

#### 4.5 Ablation Study

As our method does not introduce new deep learning modules and most hyperparameters are adopted from prior state-of-the-art [52], our ablation study focuses on our key design choices. In particular, we study: (1) the coordinate assignment strategy (Sec.3.2), where we compare keeping all points within the defined depth range versus retaining only the topmost points along height; and (2) the impact of ignoring scale in Procrustes alignment (which brings our formulation to the orthogonal Procrustes used in [52, 1]). As shown in Tab. 3, explicitly selecting the topmost points does not improve localization accuracy. The side view of an object’s top does not necessarily exhibit the most consistent semantics with the aerial image. Therefore, enforcing the use of topmost points may hinder cross-view localization. Regarding the scale-awareness, when the scale is not considered during training and testing, the model must learn feature matching that aligns strictly with the metric depth predictions. Since metric depth is imperfect, allowing the model to also estimate scale based on the matched correspondences leads to more accurate and robust local feature matching. Moreover, without modeling the scale, the method cannot support relative depth predictors [46, 45, 14], since the orthogonal Procrustes assumes that all coordinates lie in the same scale space.

Table 3: Ablation study on VIGOR same-area validation set with unknown orientation. **Best in bold.**

Method design choices	Mean loc. (m)	Median loc. (m)	Mean ori. (°)	Median ori. (°)
(1) Top points only	3.95	1.78	9.37	<b>1.77</b>
(2) Not consider scale	5.47	2.75	19.92	4.45
Ours (all points, scale-aware)	<b>3.86</b>	<b>1.75</b>	<b>9.30</b>	1.93

## 5 Conclusion

We propose a simple, accurate, and highly interpretable fine-grained cross-view localization method that matches local features between ground-level and aerial images. By leveraging monocular depth predictors, our method employs scale-aware Procrustes alignment to estimate the ground camera’s location and orientation, and optionally recover the scale between relative depth and metric space. Experiments demonstrate that our approach achieves state-of-the-art performance in challenging scenarios, including cross-area generalization and unknown camera orientation. At inference time, our model can operate with different relative depth predictors without finetuning, with only a minor impact on localization accuracy. The combination of this flexibility and consistently strong localization performance makes our method well-suited for real-world deployment.

In this Appendix, we provide the following information to support the main paper:

- A. Additional local feature matching results.
- B. Additional results on using relative depth in inference
- C. Training and testing with relative depth.
- D. Additional proof for scale-aware Procrustes alignment.
- E. Additional details on infoNCE losses.
- F. Runtime and memory usage.
- G. Limitations.
- H. Broader impact.

## A Additional Local Feature Matching Results

First, we present additional results on local feature matching. Fig. 5 shows success cases where the pose estimation is accurate, while Fig. 6 presents failure cases.

**Success cases:** In Fig. 5 (a)–(f), we demonstrate that our model effectively matches various types of road markings across views, including painted text (a)–(d) and lines (e)–(f). Notably, in Fig. 5 (b), the ‘bus’ marking is not clearly visible in the aerial view, making it difficult for humans to identify. Yet, our model successfully matches it. In general, road markings are distinctive across views, and accurately matching them significantly aids localization. When road markings are repetitive, e.g., on highways (Fig. 5 (h)), our method leverages other landmarks, such as overhead road signs and streetlights, to help anchor the keypoint locations. In urban areas, there is typically rich visual information available for matching across ground and aerial views (Fig. 5 (i)–(l)), including buildings, zebra crossings, and lane lines. Our model effectively exploits all of these cues for localization.

**Failure cases:** Typical failure cases are shown in Fig. 6. When there is dense vegetation (Fig. 6 (a)–(c)), the matchable information across views is very limited, making precise localization extremely challenging, even for humans. Interestingly, in Fig. 6 (b), our method still correctly matches the gap between two buildings in the ground view to the corresponding gap in the aerial view. In Fig. 6 (c), our method predicts a more reasonable position aligned with the path seen in the ground image, whereas the ground-truth location appears incorrect, placing the camera on the grass rather than on the path. In Fig. 6 (d), the two narrow roads with trees and a zebra crossing in front appear visually similar. At the true location, a tree partially blocks the zebra crossing in the aerial view, making it harder to distinguish. As a result, our method matches the zebra crossing to an incorrect one, leading to an erroneous location estimate. In Fig. 6 (e), although our method correctly matches the pole between the ground and aerial views, most of the scene is featureless and contains many repetitive patterns, making localization difficult. Similarly, in Fig. 6 (f), it is nearly impossible to determine the exact location over the water due to the lack of distinctive features.

We highlight again that this strong interpretability of our method stems from its explicit matches of local features, from which the output pose is analytically computed. Moreover, these matches are independent of the specific depth model used, as the depth information is only utilized when computing the pose from the correspondences.

## B Additional Results on Using Relative Depth in Inference

We conduct additional experiments on using relative depth at inference time for our model (trained with metric depth predictions from UniK3D [27]). Specifically, we use BiFuse++ [45] as our relative depth predictor for these experiments.

**Initial scale and maximum depth threshold:** As mentioned in Sec. 4.2 of the main paper, when using relative depth, we apply an initial scaling factor to all relative depth maps to bring the values into a reasonable depth range, determined by visually inspecting a few examples. We then apply a predefined maximum depth threshold, the same one used for the metric depth model, to filter out matches corresponding to sky and distant objects. In practice, the initial scale and maximum depth threshold can be determined for each dataset by visually inspecting a few examples. Here, we study how consistent the model’s predictions are when these settings are varied.

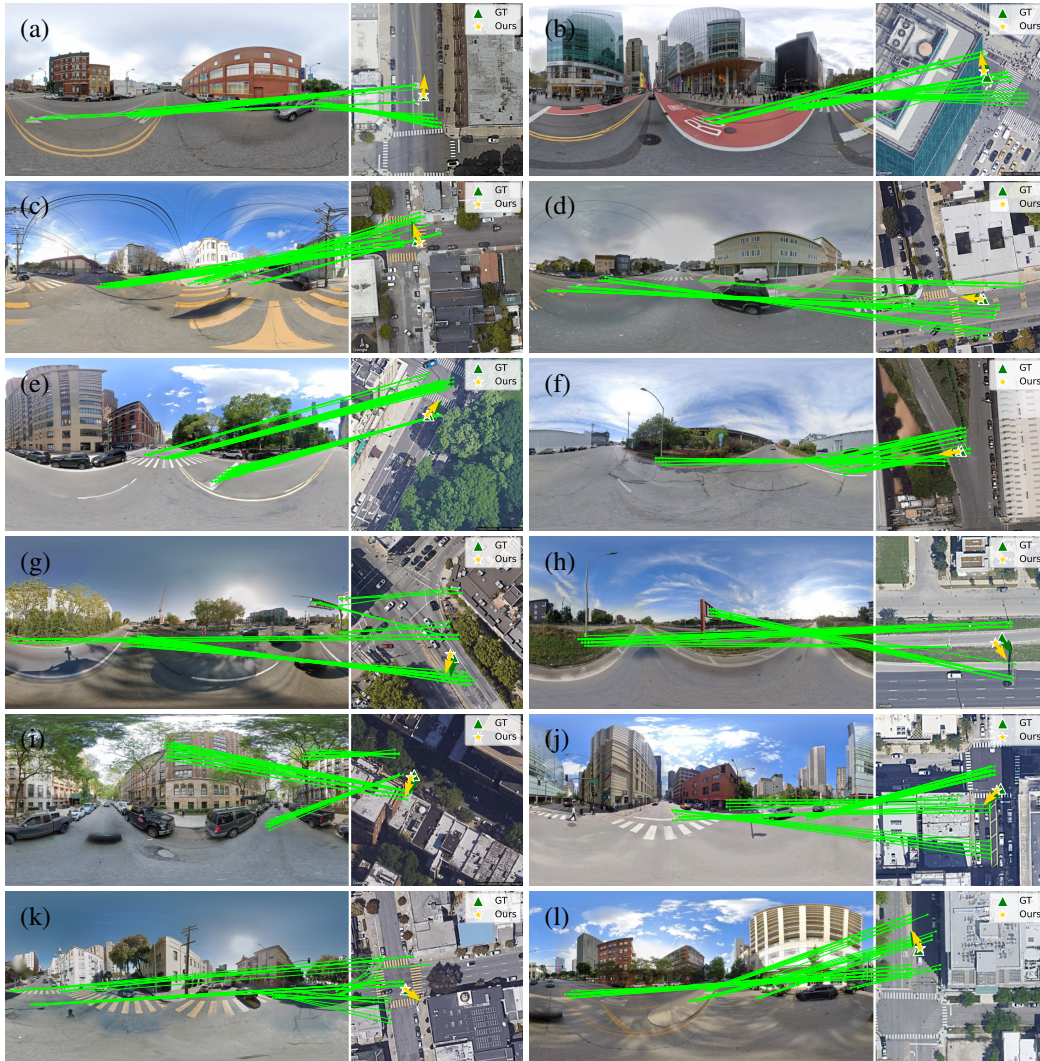


Figure 5: Success cases for localization on the VIGOR same-area test set under unknown orientation. We visualize the top 50 correspondences, ranked by matching score.

First, we evaluate the model’s robustness against different scales of the relative depth. We apply an additional scaling factor on top of the initial scale. To ensure the same objects are kept for pose estimation, the same scaling factor is also applied to the maximum depth threshold. As shown in Fig. 7, the test errors remain stable across different scaling factors during inference. This observation is consistent with our findings on applying scaling factors to metric depth in the main paper (Sec. 4.3). Therefore, in practice, when using relative depth, people do not need to carefully select an initial scale.

We then evaluate the effect of different maximum depth thresholds. Our default setting uses a threshold of 35 m, and we additionally test thresholds of 25 m and 45 m. Note that although a 35 m threshold is used during training with metric depth, applying the same 35 m threshold to relative depth does not select exactly the same set of objects, as our initial scale estimate only roughly maps the relative depth values to a reasonable range. As shown in Tab. 4, the impact of the maximum depth choice is minor, less than 0.2 m difference in localization errors. Since our feature matching is accurate, including or excluding relatively distant objects has little effect on pose estimation.

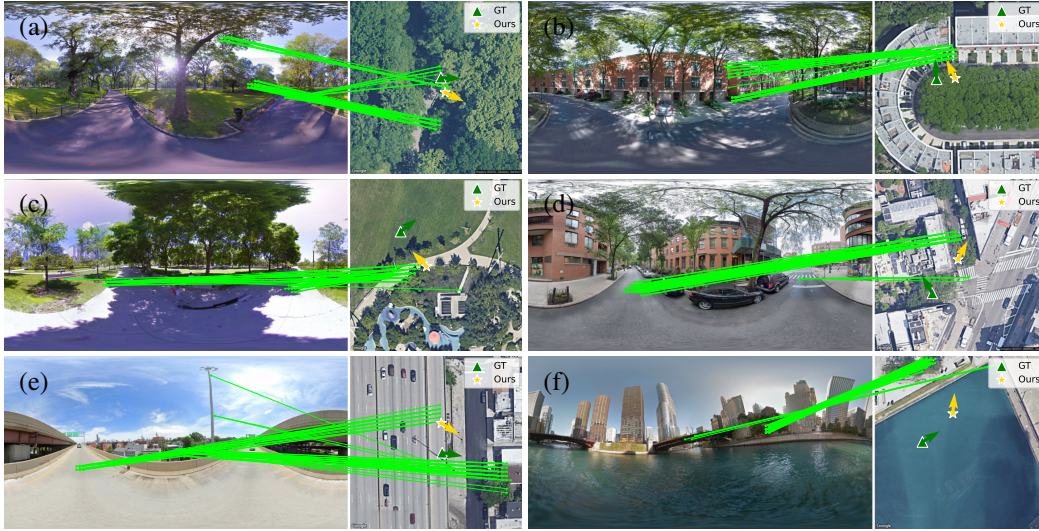


Figure 6: Failure cases for localization on the VIGOR same-area test set under unknown orientation. We visualize the top 50 correspondences, ranked by matching score.

Combined with the method’s robustness to the initial scale, this makes our approach highly practical, as users do not need to carefully select an initial scale or a depth cutoff for accurate pose estimation.

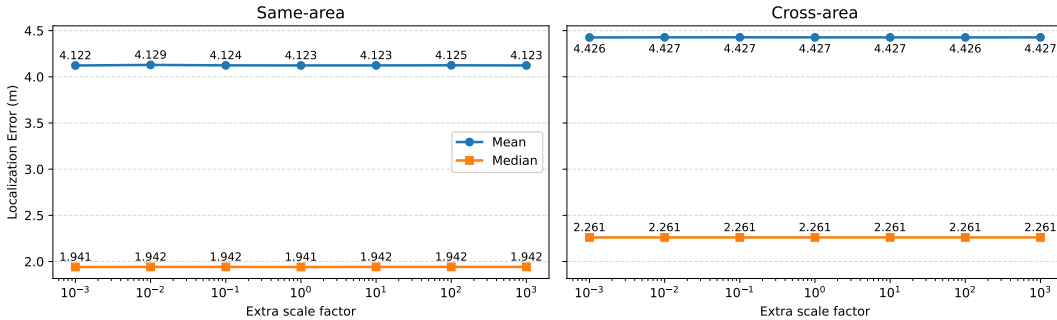


Figure 7: VIGOR test errors when different scaling factors are applied to the relative depth during inference. We use the model trained with metric depth from UniK3D [27], with unknown orientation. At inference time, we use relative depth from BiFuse++ [45].

Table 4: Robustness to different maximum depth thresholds. We apply different maximum depth thresholds during inference to remove sky and distant objects (after applying the initial scale to the relative depth from BiFuse++ [45]). Best results are shown in bold. During training, we use metric depth predictions from UniK3D[27], with a maximum depth threshold of 35 m.

Max depth	Same-area				Cross-area			
	↓ Localization (m)		↓ Orientation (°)		↓ Localization (m)		↓ Orientation (°)	
	Mean	Median	Mean	Median	Mean	Median	Mean	Median
25 m	<b>4.04</b>	<b>1.90</b>	<b>9.91</b>	<b>2.27</b>	<b>4.39</b>	<b>2.23</b>	<b>12.17</b>	<b>2.46</b>
45 m	4.20	1.97	10.46	2.35	4.47	2.27	12.30	2.51
35 m (default)	4.12	1.94	10.13	2.31	4.43	2.26	12.27	2.47

**Scale recovery:** Next, we present more results on scale recovery. Here, we apply an arbitrary initial scale to the relative depth and visualize the bird’s-eye view (BEV) points both before and after applying our estimated scale. Fig. 8 and 9 illustrate success cases. Before applying the estimated scale (third row), the BEV points clearly do not align with the aerial image. After applying the

estimated scale (fourth row), the BEV points align well with the contents in the aerial image, such as building facades and road markings. We observe that scale recovery is often reliable when the estimated pose is accurate, as both are directly derived from local feature matching, and an accurate pose results from precise local feature correspondences.

Next, we show the failure cases in Fig. 10. Sometimes, the misalignment between BEV points and the aerial image is due to the error in the estimated pose. For example, the first column of Fig. 10 shows that the scene has a symmetric layout, and our method outputs an incorrect pose by placing the BEV points at a symmetric but incorrect location. Interestingly, the transformed BEV points still align well with the aerial images, such as the zebra crossing. In the last column, the ground truth position lies on the zebra crossing, whereas the ground image indicates there is still some distance to it. Although our estimated pose deviates from the ground truth, the transformed BEV points appear to align well with the aerial image, suggesting a plausible localization despite the numerical error.

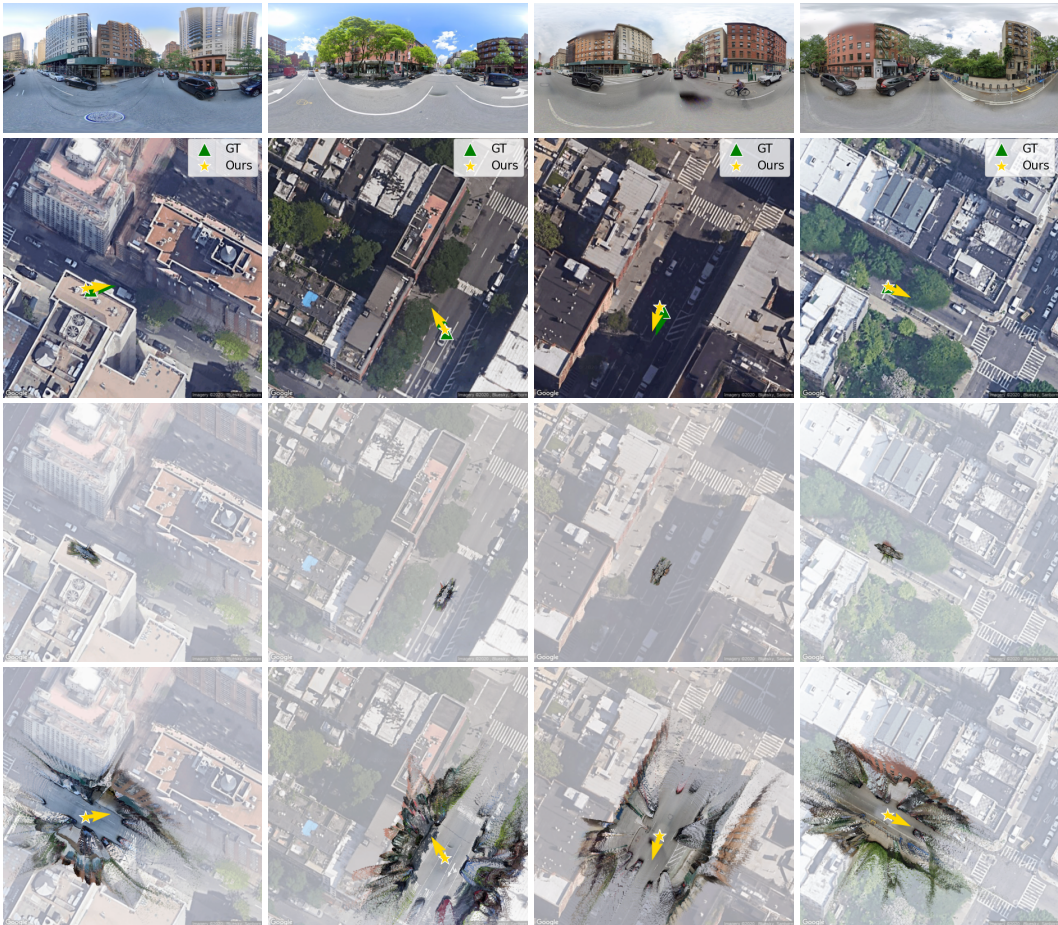


Figure 8: Success cases of scale recovery. BEV points overlaid on the aerial image after applying the predicted rotation, translation, and either the initial or predicted scale transformations. Third row: using an arbitrary initial scale. Fourth row: using the predicted scale.

### C Training and Testing with Relative Depth

As mentioned in Sec. 4.1 of the main paper, we also experimented with training and testing using only relative depth. This setup is more challenging, since inducing correct correspondences on the BEV plane requires both ground-truth pose and scale (i.e., metric depth). As a result, the infoNCE loss cannot be directly applied and we lack direct supervision of the correspondences during training.



Figure 9: Success cases of scale recovery. BEV points overlaid on the aerial image after applying the predicted rotation, translation, and either the initial or predicted scale transformations. Third row: using an arbitrary initial scale. Fourth row: using the predicted scale.

We then explored two settings. (1) Training without infoNCE losses, i.e., setting the weight  $\beta = 0$ . (2) With pseudo ground truth for infoNCE losses: At each training iteration, we estimate the scale and use it to generate pseudo ground-truth positive matches for the infoNCE losses.

As expected, using relative depth during training leads to worse performance than using metric depth (see Tab. 5). When the orientation is known, finding correct correspondences between ground and aerial images is easier. In this setting, the estimated scale may quickly converge to a reasonable range, and using it to supervise correspondences ( $\beta = 1$ ) results in better performance compared to not using it ( $\beta = 0$ ). In contrast, when the orientation is unknown, identifying correct matches becomes significantly more difficult, making it hard to recover the correct scale. In this case, incorporating the infoNCE loss ( $\beta = 1$ ) can introduce conflicting gradients to the pose supervision: correspondences derived from an inaccurate scale may reinforce incorrect matches, thereby degrading pose estimation performance.

As shown in Fig.11, without explicit supervision on the correspondences ( $\beta = 0$ ), our model still learns to establish accurate local feature matches across views. It demonstrates strong semantic understanding. For example, in Fig.11(d), different points on the streetlight in the ground view are correctly matched to the corresponding BEV of the streetlight in the aerial view.



Figure 10: Failure cases of scale recovery. BEV points overlaid on the aerial image after applying the predicted rotation, translation, and either the initial or predicted scale transformations. Third row: using an arbitrary initial scale. Fourth row: using the predicted scale.

## D Additional Proof for Scale-Aware Procrustes Alignment

As discussed in Sec. 3.2 of the main paper, we estimate pose and scale using scale-aware Procrustes alignment [43]. Here, we provide the proof of the two main steps involved:

- (1) The rotation from ground points to aerial points is computed as  $\mathbf{R} = \mathbf{V}\mathbf{U}^\top$ .
- (2) When the ground points lie in the same metric space as the aerial points, i.e., there is no scale difference between them, we have  $\text{Tr}(\mathbf{\Sigma}) = \sum_{n=1}^N w_n \left\| \tilde{\mathbf{P}}_n \right\|^2$ .

First, we recall the key notations: The inputs to the scale-aware Procrustes alignment are the coordinates of ground–aerial correspondences along with their weights. We denote the ground points as  $\mathbf{P}$ , the aerial points as  $\mathbf{Q}$ , and the weight of the  $n$ -th correspondence as  $w_n$ . The objective is to find the optimal rotation  $\mathbf{R}$ , translation  $\mathbf{t}$ , and scale  $s$  such that  $\mathbf{Q} = s(\mathbf{R} \cdot \mathbf{P}) + \mathbf{t}$ . We denote the weighted centroids of the aerial and ground point sets as  $\tilde{\mathbf{Q}}$  and  $\tilde{\mathbf{P}}$ , and the centered point sets as  $\tilde{\mathbf{Q}}$  and  $\tilde{\mathbf{P}}$ , respectively.

**(1) Rotation computation:** The optimal rotation between the ground and aerial points is independent of their relative scale and translation. Therefore, it is computed using only the centered point sets,  $\tilde{\mathbf{Q}}$

Table 5: VIGOR test results. **Best in bold.** (1) and (2): Training and testing with relative depth predicted by BiFuse++[45]. For reference, we also include the model trained and tested with metric depth from Unik3D[27], as well as the model trained with metric depth and tested with relative depth.

Ori.	Settings	Same-area				Cross-area			
		↓ Localization (m)		↓ Orientation (°)		↓ Localization (m)		↓ Orientation (°)	
		Mean	Median	Mean	Median	Mean	Median	Mean	Median
Known	(1) $\beta = 0$	3.85	2.33	-	-	4.37	2.74	-	-
	(2) $\beta = 1$	3.34	1.99	-	-	3.92	2.39	-	-
	Metric	<b>3.06</b>	<b>1.59</b>	-	-	<b>3.43</b>	<b>1.90</b>	-	-
	Metric + rel.	3.17	1.69	-	-	3.56	2.02	-	-
Unknown	(1) $\beta = 0$	5.86	3.83	23.09	9.29	6.72	4.57	29.44	12.77
	(2) $\beta = 1$	6.25	4.31	33.40	16.05	7.28	4.96	41.05	20.44
	Metric	<b>3.94</b>	<b>1.78</b>	<b>9.54</b>	<b>2.00</b>	<b>4.23</b>	<b>2.09</b>	<b>11.67</b>	<b>2.21</b>
	Metric + rel.	4.12	1.94	10.13	2.31	4.43	2.26	12.27	2.47

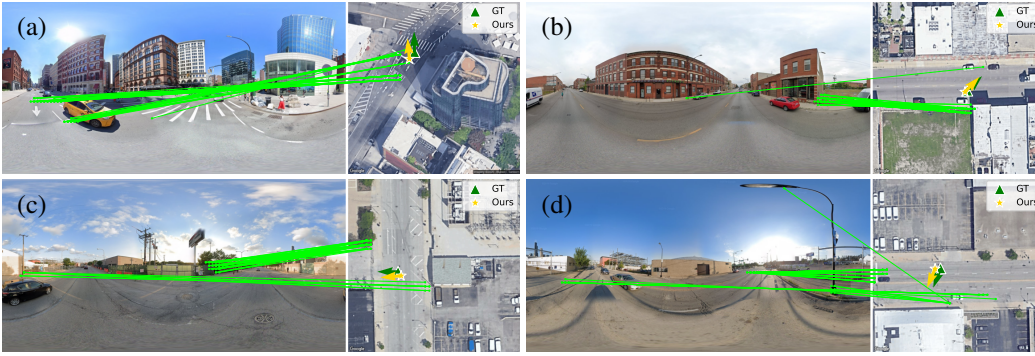


Figure 11: Local feature matching results on the VIGOR same-area test set under unknown orientation. We visualize the top 50 correspondences, ranked by matching score. The model train and test with relative depth.

and  $\tilde{\mathbf{P}}$ . We express the objective function as:

$$\mathbf{R}^* = \arg \min_{\mathbf{R}} \sum_n w_n \left\| \mathbf{R} \cdot \tilde{\mathbf{P}}_n - \tilde{\mathbf{Q}}_n \right\|^2. \quad (7)$$

In Eq. 7, the term  $\left\| \mathbf{R} \cdot \tilde{\mathbf{P}}_n - \tilde{\mathbf{Q}}_n \right\|^2$  can be rewritten as (for simplicity, we omit the explicit dot product notation):

$$\begin{aligned} \left\| \mathbf{R} \tilde{\mathbf{P}}_n - \tilde{\mathbf{Q}}_n \right\|^2 &= \left( \mathbf{R} \tilde{\mathbf{P}}_n - \tilde{\mathbf{Q}}_n \right)^\top \left( \mathbf{R} \tilde{\mathbf{P}}_n - \tilde{\mathbf{Q}}_n \right) \\ &= \left( \tilde{\mathbf{P}}_n^\top \mathbf{R}^\top - \tilde{\mathbf{Q}}_n^\top \right) \left( \mathbf{R} \tilde{\mathbf{P}}_n - \tilde{\mathbf{Q}}_n \right) \\ &= \tilde{\mathbf{P}}_n^\top \mathbf{R}^\top \mathbf{R} \tilde{\mathbf{P}}_n - \tilde{\mathbf{Q}}_n^\top \mathbf{R} \tilde{\mathbf{P}}_n - \tilde{\mathbf{P}}_n^\top \mathbf{R}^\top \tilde{\mathbf{Q}}_n + \tilde{\mathbf{Q}}_n^\top \tilde{\mathbf{Q}}_n \\ &= \left\| \tilde{\mathbf{P}}_n \right\|^2 + \left\| \tilde{\mathbf{Q}}_n \right\|^2 - 2 \tilde{\mathbf{Q}}_n^\top \mathbf{R} \tilde{\mathbf{P}}_n. \end{aligned}$$

Note that  $\left\| \tilde{\mathbf{P}}_n \right\|^2$  and  $\left\| \tilde{\mathbf{Q}}_n \right\|^2$  are fixed, and finding the optimal rotation effectively depends only on the term  $\tilde{\mathbf{Q}}_n^\top \mathbf{R} \tilde{\mathbf{P}}_n$ . Then, the objective in Eq. 7, which sums over each point correspondence, can be rewritten in matrix form as:

$$\mathbf{R}^* = \arg \max_{\mathbf{R}} \sum_n (w_n (\tilde{\mathbf{Q}}_n)^\top \mathbf{R} \tilde{\mathbf{P}}_n) \quad (8)$$

$$= \arg \max_{\mathbf{R}} \text{Tr}(\tilde{\mathbf{Q}}^\top \mathbf{R} \tilde{\mathbf{P}} \mathbf{W}) \quad (9)$$

$$= \arg \max_{\mathbf{R}} \text{Tr}(\mathbf{R} (\tilde{\mathbf{P}} \mathbf{W} \tilde{\mathbf{Q}}^\top)). \quad (10)$$

where  $\mathbf{W}$  is a diagonal matrix with each element  $W_{n,n} = w_n$ . In Eq. 10, the matrix product  $\tilde{\mathbf{P}} \mathbf{W} \tilde{\mathbf{Q}}^\top$  constructs a  $2 \times 2$  square matrix  $\mathbf{C}$ , which can be decomposed using singular value decomposition (SVD) as  $\mathbf{C} = \mathbf{U} \mathbf{\Sigma} \mathbf{V}^\top$ . Accordingly, the objective function in Eq. 10 can be reformulated as:

$$\mathbf{R}^* = \arg \max_{\mathbf{R}} \text{Tr}(\mathbf{R} (\mathbf{U} \mathbf{\Sigma} \mathbf{V}^\top)) \quad (11)$$

$$= \arg \max_{\mathbf{R}} \text{Tr}(\mathbf{\Sigma} \mathbf{V}^\top \mathbf{R} \mathbf{U}). \quad (12)$$

Since  $\mathbf{\Sigma}$  is a  $2 \times 2$  diagonal matrix with nonnegative elements, the optimal rotation is achieved when  $\mathbf{V}^\top \mathbf{R} \mathbf{U} = \mathbf{I}$ , where  $\mathbf{R} = \mathbf{V} \mathbf{U}^\top$ .

**(2) Scale computation:** As mentioned above, the  $2 \times 2$  square matrix  $\mathbf{C}$  obtained from the matrix product  $\tilde{\mathbf{P}} \mathbf{W} \tilde{\mathbf{Q}}^\top$  can also be formulated as:

$$\mathbf{C} = \sum_{n=1}^N w_n (\tilde{\mathbf{P}}_n) (\tilde{\mathbf{Q}}_n)^\top = \mathbf{U} \mathbf{\Sigma} \mathbf{V}^\top. \quad (13)$$

The centered target points  $\tilde{\mathbf{Q}}_n$  can be obtained by rotating and scaling the centered source points  $\tilde{\mathbf{P}}_n$ , satisfying  $\tilde{\mathbf{Q}}_n = s \mathbf{R} \tilde{\mathbf{P}}_n$ . Since we have already estimated the rotation  $\mathbf{R} = \mathbf{V} \mathbf{U}^\top$ , Eq. 13 can be formulated as

$$\sum_{n=1}^N w_n (\tilde{\mathbf{P}}_n) (s \mathbf{V} \mathbf{U}^\top \tilde{\mathbf{P}}_n)^\top = \mathbf{U} \mathbf{\Sigma} \mathbf{V}^\top, \quad (14)$$

$$s \sum_{n=1}^N w_n (\tilde{\mathbf{P}}_n \tilde{\mathbf{P}}_n^\top \mathbf{U} \mathbf{V}^\top) = \mathbf{U} \mathbf{\Sigma} \mathbf{V}^\top, \quad (15)$$

$$s \sum_{n=1}^N w_n (\mathbf{U}^\top \tilde{\mathbf{P}}_n \tilde{\mathbf{P}}_n^\top \mathbf{U}) = \mathbf{\Sigma}. \quad (16)$$

Then we take the trace of both sides of Eq. 16 as

$$s \text{Tr} \left( \sum_{n=1}^N w_n (\mathbf{U}^\top \tilde{\mathbf{P}}_n \tilde{\mathbf{P}}_n^\top \mathbf{U}) \right) = \text{Tr}(\mathbf{\Sigma}), \quad (17)$$

$$s \text{Tr} \left( \sum_{n=1}^N w_n (\tilde{\mathbf{P}}_n \tilde{\mathbf{P}}_n^\top \mathbf{U} \mathbf{U}^\top) \right) = \text{Tr}(\mathbf{\Sigma}). \quad (18)$$

The trace of  $\tilde{\mathbf{P}}_n \tilde{\mathbf{P}}_n^\top$  is equivalent to the norm of  $\tilde{\mathbf{P}}_n$ . Thus, the scale  $s$  can be computed by

$$s \sum_{n=1}^N w_n \|\tilde{\mathbf{P}}_n\|^2 = \text{Tr}(\mathbf{\Sigma}), \quad (19)$$

$$s = \frac{\text{Tr}(\mathbf{\Sigma})}{\sum_{n=1}^N w_n \|\tilde{\mathbf{P}}_n\|^2}. \quad (20)$$

Hence, when  $s = 1$ , we have  $\text{Tr}(\mathbf{\Sigma}) = \sum_{n=1}^N w_n \|\tilde{\mathbf{P}}_n\|^2$ .

## E Additional Details on InfoNCE Losses

Here, we provide details on the applied infoNCE losses,  $\mathcal{L}_{G2S}$  and  $\mathcal{L}_{S2G}$ . These losses encourage correspondences that align with the ground-truth pose while discouraging incorrect matches.

Given the sampled  $N$  corresponding ground points  $\mathbf{P}$  and aerial points  $\mathbf{Q}$ , we compute the true aerial correspondences for  $\mathbf{P}$  as  $\hat{\mathbf{Q}} = s(\mathbf{R}_{\text{gt}} \cdot \mathbf{P}) + \mathbf{t}_{\text{gt}}$ , the true ground correspondences for  $\mathbf{Q}$  as  $\hat{\mathbf{P}} = \mathbf{R}_{\text{gt}}^T \cdot ((\mathbf{Q} - \mathbf{t}_{\text{gt}})/s)$ , and  $s = 1$  when we use metric depth during training. Then, we find in the pairwise matching score matrix  $M$  for the scores for these correspondences, denoting as  $M^{\mathbf{P},\hat{\mathbf{Q}}}$  and  $M^{\hat{\mathbf{P}},\mathbf{Q}}$ , which will serve as the positives in the infoNCE loss.

Assuming there are  $N_{\mathbf{P}}$  valid scores in  $M^{\mathbf{P},\hat{\mathbf{Q}}}$  (excluding points whose correspondences fall outside the aerial image), and denoting the  $n$ -th score as  $M_n^{\mathbf{P},\hat{\mathbf{Q}}}$ , the loss  $\mathcal{L}_{G2S}$  is computed as:

$$\mathcal{L}_{G2S} = -\frac{1}{N_{\mathbf{P}}} \sum_{n=1}^{N_{\mathbf{P}}} \log \frac{e^{M_n^{\mathbf{P},\hat{\mathbf{Q}}}}}{\sum e^{M_i}}, \quad (21)$$

where  $M_i$  is the  $i$ -th column correspond to the current ground point in the pairwise matching score matrix  $M$ . Essentially,  $\mathcal{L}_{G2S}$  encourages each sampled ground point to match the aerial point found by the ground-truth pose and scale, while discouraging matches to all other aerial points.

For  $\mathcal{L}_{S2G}$ , we do not simply encourage the matching score  $M^{\mathbf{Q},\hat{\mathbf{P}}}$  while discouraging all other matches. This is because multiple ground points may share similar planar coordinates but differ in height (i.e., the  $z$  coordinate). As described in Section 3.3 of the main paper, we define a local neighborhood and use only matching scores correspond to ground points outside this neighborhood as negatives. The loss  $\mathcal{L}_{S2G}$  is then computed as:

$$\mathcal{L}_{S2G} = -\frac{1}{N_{\mathbf{Q}}} \sum_{n=1}^{N_{\mathbf{Q}}} \log \frac{e^{M_n^{\mathbf{Q},\hat{\mathbf{P}}}}}{\sum e^{M_{\text{neg}}}}, \quad (22)$$

where  $N_{\mathbf{Q}}$  is the number of valid scores in  $M^{\mathbf{Q},\hat{\mathbf{P}}}$ , and  $M_{\text{neg}}$  are the negatives for each sampled aerial point.

## F Runtime and Memory Usage

Next, we report the runtime and memory usage of our method on VIGOR.

**Runtime:** On a single H100 GPU, our method achieves 14.74 FPS without RANSAC [8] (0.03s for our model and 0.04s for the depth predictor Unik3D [27]) and 0.42 FPS with RANSAC. This is faster than the previous local feature matching method FG<sup>2</sup> [52], which runs at 9.26 FPS without RANSAC and 0.32 FPS with it. Notably, when prioritizing speed, omitting RANSAC results in only a small increase in localization error, e.g., on VIGOR same-area test set with known orientation the mean error increases from 3.06 m to 3.29 m. Furthermore, one can use a faster depth predictor to further reduce inference time.

**Memory:** our model uses 726.74 MB, with 580.54 MB for the frozen DINOv2 [25], while the metric depth predictor Unik3D [27] uses 1368.81 MB.

## G Limitations

As stated in Sec. 3.2 of the main paper, our method is based on the assumption that the transformation between aerial and ground points can be modeled as a similarity transform. However, aerial images in existing datasets are often not orthorectified. For instance, building facades are visible in some aerial views, indicating perspective distortions. Consequently, the relationship between aerial points and BEV ground points may deviate from a true similarity transformation. Additionally, our pose estimation depends on an external depth predictor. Inaccuracies in the predicted depth maps can directly affect the precision of the estimated poses, potentially leading to degraded localization performance. Still, we experimentally show that, under the assumption of a similarity transformation, using off-the-shelf depth predictors can yield satisfactory localization performance.

## H Broader Impact

Fine-grained cross-view localization has the potential to significantly advance a wide range of real-world applications. In domains such as autonomous driving, robotics, and augmented reality, accurate and reliable localization is essential. Our method offers enhanced robustness and precision in scenarios where specialized sensors are unreliable, such as GNSS in urban canyons. However, we also acknowledge potential risks. Fine-grained localization could be misused for surveillance or unauthorized tracking if deployed without appropriate safeguards. We recommend that future deployments include rigorous ethical guidelines and privacy-preserving mechanisms.

## References

- [1] Axel Barroso-Laguna, Sowmya Munukutla, Victor Adrian Prisacariu, and Eric Brachmann. Matching 2d images in 3d: Metric relative pose from metric correspondences. In *Proceedings of the IEEE/CVF Conference on Computer Vision and Pattern Recognition*, pages 4852–4863, 2024.
- [2] Shariq Farooq Bhat, Reiner Birkel, Diana Wofk, Peter Wonka, and Matthias Müller. Zoedepth: Zero-shot transfer by combining relative and metric depth. *arXiv preprint arXiv:2302.12288*, 2023.
- [3] Daniel DeTone, Tomasz Malisiewicz, and Andrew Rabinovich. Superpoint: Self-supervised interest point detection and description. In *Proceedings of the IEEE Conference on Computer Vision and Pattern Recognition Workshops*, pages 224–236, 2018.
- [4] Yaqing Ding, Václav Vávra, Snehal Bhayani, Qianliang Wu, Jian Yang, and Zuzana Kukelova. Fundamental matrix estimation using relative depths. In *European Conference on Computer Vision*, pages 142–159. Springer, 2024.
- [5] David Eigen, Christian Puhrsch, and Rob Fergus. Depth map prediction from a single image using a multi-scale deep network. *Advances in Neural Information Processing Systems*, 27, 2014.
- [6] Florian Fervers, Sebastian Bullinger, Christoph Bodensteiner, Michael Arens, and Rainer Stiefelhagen. C-bev: Contrastive bird’s eye view training for cross-view image retrieval and 3-dof pose estimation. *arXiv preprint arXiv:2312.08060*, 2023.
- [7] Florian Fervers, Sebastian Bullinger, Christoph Bodensteiner, Michael Arens, and Rainer Stiefelhagen. Uncertainty-aware vision-based metric cross-view geolocalization. In *Proceedings of the IEEE/CVF Conference on Computer Vision and Pattern Recognition*, pages 21621–21631, 2023.
- [8] Martin A Fischler and Robert C Bolles. Random sample consensus: a paradigm for model fitting with applications to image analysis and automated cartography. *Communications of the ACM*, 24(6):381–395, 1981.
- [9] Huan Fu, Mingming Gong, Chaohui Wang, Kayhan Batmanghelich, and Dacheng Tao. Deep ordinal regression network for monocular depth estimation. In *Proceedings of the IEEE conference on computer vision and pattern recognition*, pages 2002–2011, 2018.
- [10] Andreas Geiger, Philip Lenz, Christoph Stiller, and Raquel Urtasun. Vision meets robotics: The kitti dataset. *International Journal of Robotics Research*, 2013.
- [11] Google. Google maps static api, 2024.
- [12] John C Gower. Generalized procrustes analysis. *Psychometrika*, 40:33–51, 1975.
- [13] Mu Hu, Wei Yin, Chi Zhang, Zhipeng Cai, Xiaoxiao Long, Hao Chen, Kaixuan Wang, Gang Yu, Chunhua Shen, and Shaojie Shen. Metric3d v2: A versatile monocular geometric foundation model for zero-shot metric depth and surface normal estimation. *IEEE Transactions on Pattern Analysis and Machine Intelligence*, 2024.
- [14] Hualie Jiang, Zhe Sheng, Siyu Zhu, Zilong Dong, and Rui Huang. Unifuse: Unidirectional fusion for 360 panorama depth estimation. *IEEE Robotics and Automation Letters*, 6(2):1519–1526, 2021.
- [15] Wooju Lee, Juhye Park, Dasol Hong, Changki Sung, Youngwoo Seo, Dongwan Kang, and Hyun Myung. Pidloc: Cross-view pose optimization network inspired by pid controllers. *arXiv preprint arXiv:2503.02388*, 2025.

- [16] Ted Lentsch, Zimin Xia, Holger Caesar, and Julian FP Kooij. Slicematch: Geometry-guided aggregation for cross-view pose estimation. In *Proceedings of the IEEE/CVF Conference on Computer Vision and Pattern Recognition*, pages 17225–17234, 2023.
- [17] Vincent Lepetit, Francesc Moreno-Noguer, and Pascal Fua. Ep n p: An accurate o (n) solution to the p n p problem. *International Journal of Computer Vision*, 81:155–166, 2009.
- [18] Kunpeng Li, Yulun Zhang, Kai Li, Yuanyuan Li, and Yun Fu. Visual semantic reasoning for image-text matching. In *Proceedings of the IEEE/CVF International Conference on Computer Vision*, pages 4654–4662, 2019.
- [19] Ruibo Li, Ke Xian, Chunhua Shen, Zhiguo Cao, Hao Lu, and Lingxiao Hang. Deep attention-based classification network for robust depth prediction. In C.V. Jawahar, Hongdong Li, Greg Mori, and Konrad Schindler, editors, *Computer Vision – ACCV 2018*, pages 663–678, Cham, 2019. Springer International Publishing.
- [20] Zhengqi Li and Noah Snavely. Megadepth: Learning single-view depth prediction from internet photos. In *Computer Vision and Pattern Recognition (CVPR)*, 2018.
- [21] Fayao Liu, Chunhua Shen, and Guosheng Lin. Deep convolutional neural fields for depth estimation from a single image. In *Proceedings of the IEEE conference on computer vision and pattern recognition*, pages 5162–5170, 2015.
- [22] Ilya Loshchilov and Frank Hutter. Decoupled weight decay regularization. In *International Conference on Learning Representations*, 2019. URL <https://openreview.net/forum?id=Bkg6RiCqY7>.
- [23] Pushmeet Kohli Nathan Silberman, Derek Hoiem and Rob Fergus. Indoor segmentation and support inference from rgbd images. In *ECCV*, 2012.
- [24] Aaron van den Oord, Yazhe Li, and Oriol Vinyals. Representation learning with contrastive predictive coding. *arXiv preprint arXiv:1807.03748*, 2018.
- [25] Maxime Oquab, Timothée Darcet, Théo Moutakanni, Huy V. Vo, Marc Szafraniec, Vasil Khalidov, Pierre Fernandez, Daniel HAZIZA, Francisco Massa, Alaaeldin El-Nouby, Mido Assran, Nicolas Ballas, Wojciech Galuba, Russell Howes, Po-Yao Huang, Shang-Wen Li, Ishan Misra, Michael Rabbat, Vasu Sharma, Gabriel Synnaeve, Hu Xu, Herve Jegou, Julien Mairal, Patrick Labatut, Armand Joulin, and Piotr Bojanowski. DINOv2: Learning robust visual features without supervision. *Transactions on Machine Learning Research*, 2024. ISSN 2835-8856. URL <https://openreview.net/forum?id=a68SUt6zFt>.
- [26] Luigi Piccinelli, Yung-Hsu Yang, Christos Sakaridis, Mattia Segu, Siyuan Li, Luc Van Gool, and Fisher Yu. UniDepth: Universal monocular metric depth estimation. In *Proceedings of the IEEE/CVF Conference on Computer Vision and Pattern Recognition (CVPR)*, 2024.
- [27] Luigi Piccinelli, Christos Sakaridis, Mattia Segu, Yung-Hsu Yang, Siyuan Li, Wim Abbeloos, and Luc Van Gool. Unik3d: Universal camera monocular 3d estimation. *arXiv preprint arXiv:2503.16591*, 2025.
- [28] René Ranftl, Alexey Bochkovskiy, and Vladlen Koltun. Vision transformers for dense prediction. *ArXiv preprint*, 2021.
- [29] René Ranftl, Katrin Lasinger, David Hafner, Konrad Schindler, and Vladlen Koltun. Towards robust monocular depth estimation: Mixing datasets for zero-shot cross-dataset transfer. *IEEE Transactions on Pattern Analysis and Machine Intelligence*, 44(3), 2022.
- [30] Jiangwei Ren, Xingyu Jiang, Zizhuo Li, Dingkan Liang, Xin Zhou, and Xiang Bai. Minima: Modality invariant image matching. *arXiv preprint arXiv:2412.19412*, 2024.
- [31] Anirban Roy and Sinisa Todorovic. Monocular depth estimation using neural regression forest. In *Proceedings of the IEEE conference on computer vision and pattern recognition*, pages 5506–5514, 2016.
- [32] Paul-Edouard Sarlin, Cesar Cadena, Roland Siegwart, and Marcin Dymczyk. From coarse to fine: Robust hierarchical localization at large scale. In *Proceedings of the IEEE/CVF Conference on Computer Vision and Pattern Recognition*, pages 12716–12725, 2019.
- [33] Paul-Edouard Sarlin, Daniel DeTone, Tomasz Malisiewicz, and Andrew Rabinovich. Superglue: Learning feature matching with graph neural networks. In *Proceedings of the IEEE/CVF Conference on Computer Vision and Pattern Recognition*, pages 4938–4947, 2020.
- [34] Paul-Edouard Sarlin, Eduard Trulls, Marc Pollefeys, Jan Hosang, and Simon Lymen. Snap: Self-supervised neural maps for visual positioning and semantic understanding. *Advances in Neural Information Processing Systems*, 36, 2024.

- [35] Torsten Sattler, Bastian Leibe, and Leif Kobbelt. Efficient & effective prioritized matching for large-scale image-based localization. *IEEE Transactions on Pattern Analysis and Machine Intelligence*, 39(9): 1744–1756, 2016.
- [36] Yujiao Shi and Hongdong Li. Beyond cross-view image retrieval: Highly accurate vehicle localization using satellite image. In *Proceedings of the IEEE/CVF Conference on Computer Vision and Pattern Recognition*, pages 17010–17020, 2022.
- [37] Yujiao Shi, Fei Wu, Akhil Perincherry, Ankit Vora, and Hongdong Li. Boosting 3-dof ground-to-satellite camera localization accuracy via geometry-guided cross-view transformer. In *Proceedings of the IEEE/CVF International Conference on Computer Vision*, pages 21516–21526, 2023.
- [38] Zhenbo Song, Xianghui Ze, Jianfeng Lu, and Yujiao Shi. Learning dense flow field for highly-accurate cross-view camera localization. *Advances in Neural Information Processing Systems*, 36, 2024.
- [39] Ziyang Song, Zerong Wang, Bo Li, Hao Zhang, Ruijie Zhu, Li Liu, Peng-Tao Jiang, and Tianzhu Zhang. Depthmaster: Taming diffusion models for monocular depth estimation. *arXiv preprint arXiv:2501.02576*, 2025.
- [40] J. Sturm, N. Engelhard, F. Endres, W. Burgard, and D. Cremers. A benchmark for the evaluation of rgb-d slam systems. In *Proc. of the International Conference on Intelligent Robot Systems (IROS)*, Oct. 2012.
- [41] Jiaming Sun, Zehong Shen, Yuang Wang, Hujun Bao, and Xiaowei Zhou. Loftr: Detector-free local feature matching with transformers. In *Proceedings of the IEEE/CVF Conference on Computer Vision and Pattern Recognition*, pages 8922–8931, 2021.
- [42] Sebastian Thrun. Probabilistic robotics. *Communications of the ACM*, 45(3):52–57, 2002.
- [43] Shinji Umeyama. Least-squares estimation of transformation parameters between two point patterns. *IEEE Transactions on Pattern Analysis & Machine Intelligence*, 13(04):376–380, 1991.
- [44] Ashish Vaswani, Noam Shazeer, Niki Parmar, Jakob Uszkoreit, Llion Jones, Aidan N Gomez, Łukasz Kaiser, and Illia Polosukhin. Attention is all you need. *Advances in Neural Information Processing Systems*, 30, 2017.
- [45] Fu-En Wang, Yu-Hsuan Yeh, Yi-Hsuan Tsai, Wei-Chen Chiu, and Min Sun. Bifuse++: Self-supervised and efficient bi-projection fusion for 360 depth estimation. *IEEE Transactions on Pattern Analysis and Machine Intelligence*, 45(5):5448–5460, 2022.
- [46] Ning-Hsu Albert Wang and Yu-Lun Liu. Depth anywhere: Enhancing 360 monocular depth estimation via perspective distillation and unlabeled data augmentation. *Advances in Neural Information Processing Systems*, 37:127739–127764, 2024.
- [47] Qiwei Wang, Shaoxun Wu, and Yujiao Shi. Bevspat: Resolving height ambiguity via feature-based gaussian primitives for weakly-supervised cross-view localization. *arXiv preprint arXiv:2502.09080*, 2025.
- [48] Shan Wang, Yanhao Zhang, Akhil Perincherry, Ankit Vora, and Hongdong Li. View consistent purification for accurate cross-view localization. In *Proceedings of the IEEE/CVF International Conference on Computer Vision*, pages 8197–8206, 2023.
- [49] Shan Wang, Yanhao Zhang, Ankit Vora, Akhil Perincherry, and Hengdong Li. Satellite image based cross-view localization for autonomous vehicle. In *IEEE International Conference on Robotics and Automation*, pages 3592–3599. IEEE, 2023.
- [50] Shan Wang, Chuong Nguyen, Jiawei Liu, Yanhao Zhang, Sundaram Muthu, Fahira Afzal Maken, Kaihao Zhang, and Hongdong Li. View from above: Orthogonal-view aware cross-view localization. In *Proceedings of the IEEE/CVF Conference on Computer Vision and Pattern Recognition*, pages 14843–14852, 2024.
- [51] Xiaolong Wang, Runsen Xu, Zhuofan Cui, Zeyu Wan, and Yu Zhang. Fine-grained cross-view geo-localization using a correlation-aware homography estimator. *Advances in Neural Information Processing Systems*, 36, 2024.
- [52] Zimin Xia and Alexandre Alahi. Fg<sup>2</sup>: Fine-grained cross-view localization by fine-grained feature matching. *arXiv preprint arXiv:2503.18725*, 2025.
- [53] Zimin Xia, Olaf Booij, Marco Manfredi, and Julian F. P. Kooij. Cross-view matching for vehicle localization by learning geographically local representations. *IEEE Robotics and Automation Letters*, 6(3):5921–5928, 2021. doi: 10.1109/LRA.2021.3088076.

- [54] Zimin Xia, Olaf Booij, Marco Manfredi, and Julian FP Kooij. Visual cross-view metric localization with dense uncertainty estimates. In *European Conference on Computer Vision*, pages 90–106. Springer, 2022.
- [55] Zimin Xia, Olaf Booij, and Julian FP Kooij. Convolutional cross-view pose estimation. *IEEE Transactions on Pattern Analysis and Machine Intelligence*, 2023.
- [56] Shuanglin Yan, Neng Dong, Liyan Zhang, and Jinhui Tang. Clip-driven fine-grained text-image person re-identification. *IEEE Transactions on Image Processing*, 32:6032–6046, 2023.
- [57] Li Yang, Yan Xu, Chunfeng Yuan, Wei Liu, Bing Li, and Weiming Hu. Improving visual grounding with visual-linguistic verification and iterative reasoning. In *Proceedings of the IEEE/CVF Conference on Computer Vision and Pattern Recognition*, pages 9499–9508, 2022.
- [58] Lihe Yang, Bingyi Kang, Zilong Huang, Xiaogang Xu, Jiashi Feng, and Hengshuang Zhao. Depth anything: Unleashing the power of large-scale unlabeled data. In *Proceedings of the IEEE/CVF Conference on Computer Vision and Pattern Recognition*, pages 10371–10381, 2024.
- [59] Lihe Yang, Bingyi Kang, Zilong Huang, Zhen Zhao, Xiaogang Xu, Jiashi Feng, and Hengshuang Zhao. Depth anything v2. *Advances in Neural Information Processing Systems*, 37:21875–21911, 2024.
- [60] Wei Yin, Chi Zhang, Hao Chen, Zhipeng Cai, Gang Yu, Kaixuan Wang, Xiaozhi Chen, and Chunhua Shen. Metric3d: Towards zero-shot metric 3d prediction from a single image. In *Proceedings of the IEEE/CVF International Conference on Computer Vision*, pages 9043–9053, 2023.
- [61] Yifan Yu, Shaohui Liu, Rémi Pautrat, Marc Pollefeys, and Viktor Larsson. Relative pose estimation through affine corrections of monocular depth priors. *arXiv preprint arXiv:2501.05446*, 2025.
- [62] Ruijie Zhu, Chuxin Wang, Ziyang Song, Li Liu, Tianzhu Zhang, and Yongdong Zhang. Scaledepth: Decomposing metric depth estimation into scale prediction and relative depth estimation. *arXiv preprint arXiv:2407.08187*, 2024.
- [63] Sijie Zhu, Taojiannan Yang, and Chen Chen. Vigor: Cross-view image geo-localization beyond one-to-one retrieval. In *Proceedings of the IEEE/CVF Conference on Computer Vision and Pattern Recognition*, pages 3640–3649, 2021.